A reversible oxygen redox reaction in bulk-type all-solid-state batteries

Nagao, Kenji; Nagata, Yuka; Sakuda, Atsushi; Hayashi, Akitoshi; Deguchi, Minako; Hotehama, Chie; Tsukasaki, Hirofumi; ... Yamamoto, Kentaro; Uchimoto, Yoshiharu; Tatsumisago, Masahiro

SCIENCE ADVANCES | RESEARCH ARTICLE

ELECTROCHEMISTRY

A reversible oxygen redox reaction in bulk-type all-solid-state batteries

Kenji Nagao[1], Yuka Nagata[1], Atsushi Sakuda[1]*, Akitoshi Hayashi[1], Minako Deguchi[1], Chie Hotehama[1], Hirofumi Tsukasaki[2], Shigeo Mori[2], Yuki Orikasa[3,4], Kentaro Yamamoto[5], Yoshiharu Uchimoto[5], Masahiro Tatsumisago[1]

An all-solid-state lithium battery using inorganic solid electrolytes requires safety assurance and improved energy density, both of which are issues in large-scale applications of lithium-ion batteries. Utilization of high-capacity lithium-excess electrode materials is effective for the further increase in energy density. However, they have never been applied to all-solid-state batteries. Operational difficulty of all-solid-state batteries using them generally lies in the construction of the electrode-electrolyte interface. By the amorphization of Li_2RuO_3 as a lithium-excess model material with Li_2SO_4, here, we have first demonstrated a reversible oxygen redox reaction in all-solid-state batteries. Amorphous nature of the Li_2RuO_3-Li_2SO_4 matrix enables inclusion of active material with high conductivity and ductility for achieving favorable interfaces with charge transfer capabilities, leading to the stable operation of all-solid-state batteries.

INTRODUCTION

All-solid-state lithium secondary batteries (ASSBs) have attracted great attention because of their high safety owing to the use of nonflammable inorganic solid electrolytes and their possibility to be used in a wide temperature range (*1*–*3*). In addition, a higher volumetric energy density can be achieved by stacking several cells. Solid electrolytes with an extremely high lithium ionic conductivity of more than 10^{-2} S cm^{-1} have already been discovered, with their conductivity consistently higher than that of the liquid electrolytes (*4*–*6*). Therefore, the discovery of new and efficient electrode materials is key for the construction of ASSBs with high energy density. In the electrode layers for conventional ASSBs, mixtures composed of active material, solid electrolyte, and carbon conductive additive powders are often applied to secure lithium ionic and electronic conduction pathways. Moreover, most ASSBs reported so far comprise a thin electrode layer with a small amount of active materials and a thick electrolyte layer as the separator. Therefore, the energy density of ASSBs at the present stage is considerably lower than that of typical lithium-ion batteries (LiBs). For practical application of ASSBs, substantial improvement in energy density is strongly desired. To this end, there are two possible strategies: one is utilization of high-capacity electrode materials, and the other is to increase the content of active materials in electrode layers.

Previously, typical layered compounds (e.g., $LiCoO_2$ and $LiNi_{1/3}Mn_{1/3}Co_{1/3}O_2$) (*7*, *8*) have been used as an active material in ASSBs. In the past decade, various lithium-excess compounds have been extensively studied as candidate electrode materials in LiBs because of their high capacity caused by the cumulative cationic and anionic redox reactions (*9*–*17*). Among them, Li_2RuO_3 is a representative model positive electrode material with a lithium-excess layered structure with the space group *C*2/*c* (*10*). Tarascon and colleagues (*11*–*13*) proposed the substitution of electrochemically inactive Sn^{4+} ions as a stabilizer for Ru^{4+} ions in the layered Li_2RuO_3 structure and achieved a high reversible capacity of more than 220 mAh g^{-1} of active materials. Nevertheless, application of these lithium-excess positive electrode materials to ASSBs has never been reported, probably because of side reactions with solid electrolytes that lead to poor contact and large charge transfer resistance. Demand for next-generation electrode materials in ASSBs is different from that for conventional materials in liquid-type LiBs. The most important features for the operation of ASSBs are formation of the electrode-electrolyte interface and design of favorable lithium ionic conduction pathways in the electrode layers. To obtain superior electrode/electrolyte interfaces with large contact area and good lithium ionic conduction pathways in the electrode layer, it is necessary to use large amount of highly moldable solid electrolytes. However, by increasing the amount of electrolytes, active material content should be decreased, which leads to a decrease in energy density. Therefore, development of active materials with favorable ductility and high ionic conductivity in addition to high capacity is necessary for energy density enhancement. Recently, we have proposed that incorporation of Li_2SO_4 to form an amorphous structure improves ductility and ionic conductivity of oxide glassy materials (*18*). Moreover, this strategy can be extended to electrode active materials for ASSBs (*19*–*21*). By blending Li_2SO_4 with classical transition metal oxide active materials such as $LiCoO_2$, highly ductile novel positive electrode active materials can be developed. Here, we aim to develop an active material with high ductility and high capacity suitable for ASSBs with high energy density by applying this strategy to lithium-excess transition metal oxide such as Li_2RuO_3.

With consideration to the demands and features described above, we have successfully developed a novel $Li_2Ru_{0.8}S_{0.2}O_{3.2}$ [$80Li_2RuO_3 \cdot 20Li_2SO_4$ in mole percent (mol %)] positive electrode material for ASSBs with a high reversible capacity of about 270 mAh g^{-1}. Mechanochemical treatment with Li_2SO_4 imparts ionic conductivity and favorable ductility to the Li_2RuO_3 active material. Because of the favorable

[1]Department of Applied Chemistry, Graduate School of Engineering, Osaka Prefecture University, 1-1, Gakuen-cho, Naka-ku, Sakai, Osaka 599-8531, Japan. [2]Department of Materials Science, Graduate School of Engineering, Osaka Prefecture University, 1-1, Gakuen-cho, Naka-ku, Sakai, Osaka 599-8531, Japan. [3]Department of Applied Chemistry, College of Life Science, Ritsumeikan University, 1-1-1, Noji-Higashi, Kusatsu, Shiga 525-8577, Japan. [4]SR Center, Ritsumeikan University, 1-1-1 Noji-Higashi, Kusatsu, Shiga 525-8577, Japan. [5]Graduate School of Human and Environmental Studies, Kyoto University, Nihonmatsu-cho, Yoshida, Sakyo-ku, Kyoto 606-8317, Japan.
*Corresponding author. Email: saku@chem.osakafu-u.ac.jp

ductility and high electronic and ionic conductivities, we have achieved the fabrication of ASSBs with extremely high energy density, where the positive electrode layer only used the active material without any conductive additives. This strategy in the development of positive electrode materials will contribute to discovering novel electrode materials suitable for ASSBs with high energy density. In the following section, the structure and electrochemical properties of the novel Li_2RuO_3-Li_2SO_4 positive electrode materials are discussed.

RESULTS AND DISCUSSION

Synthesis of Li_2RuO_3-Li_2SO_4 positive electrode active materials

$Li_2Ru_{0.8}S_{0.2}O_{3.2}$ ($80Li_2RuO_3{\cdot}20Li_2SO_4$ mol %) was synthesized via mechanochemistry of crystalline Li_2RuO_3 and Li_2SO_4 (Fig. 1A). Although crystalline Li_2RuO_3 has a layered structure with the space group $C2/c$ (*10*), after the ball-milling treatment of Li_2RuO_3 with Li_2SO_4, the diffraction peaks attributable to the starting materials disappeared and broad peaks appeared in the X-ray diffraction (XRD) patterns shown in Fig. 1B. These patterns can be assigned to the NaCl-type cation-disordered phase with the space group $Fm\bar{3}m$. In the layered structure of $LiCoO_2$ ($R\bar{3}m$) or Li_2RuO_3 ($C2/c$), Li^+ ions mainly migrate in two dimensions along the *ab* plane. On the other hand, in the disordered rocksalt structure, O^{2-} ions are closely packed in a face-centered cubic structure, and Li^+ and Ru^{4+} ions randomly occupy the octahedral cation site. In this structure, Li^+ ion can diffuse in three dimensions by the formation of a percolation network with excess lithium (*14*), which is an advantageous function in active electrode material. In the XRD pattern, the Bragg peak shift is not observed, even when Li_2SO_4 content is changed (fig. S1), indicating that S^{6+} ion hardly occupies the octahedral site in the rocksalt structure and that Li_2SO_4 forms amorphous phases, which is supported by the Rietveld refinement shown in fig. S1. The scanning

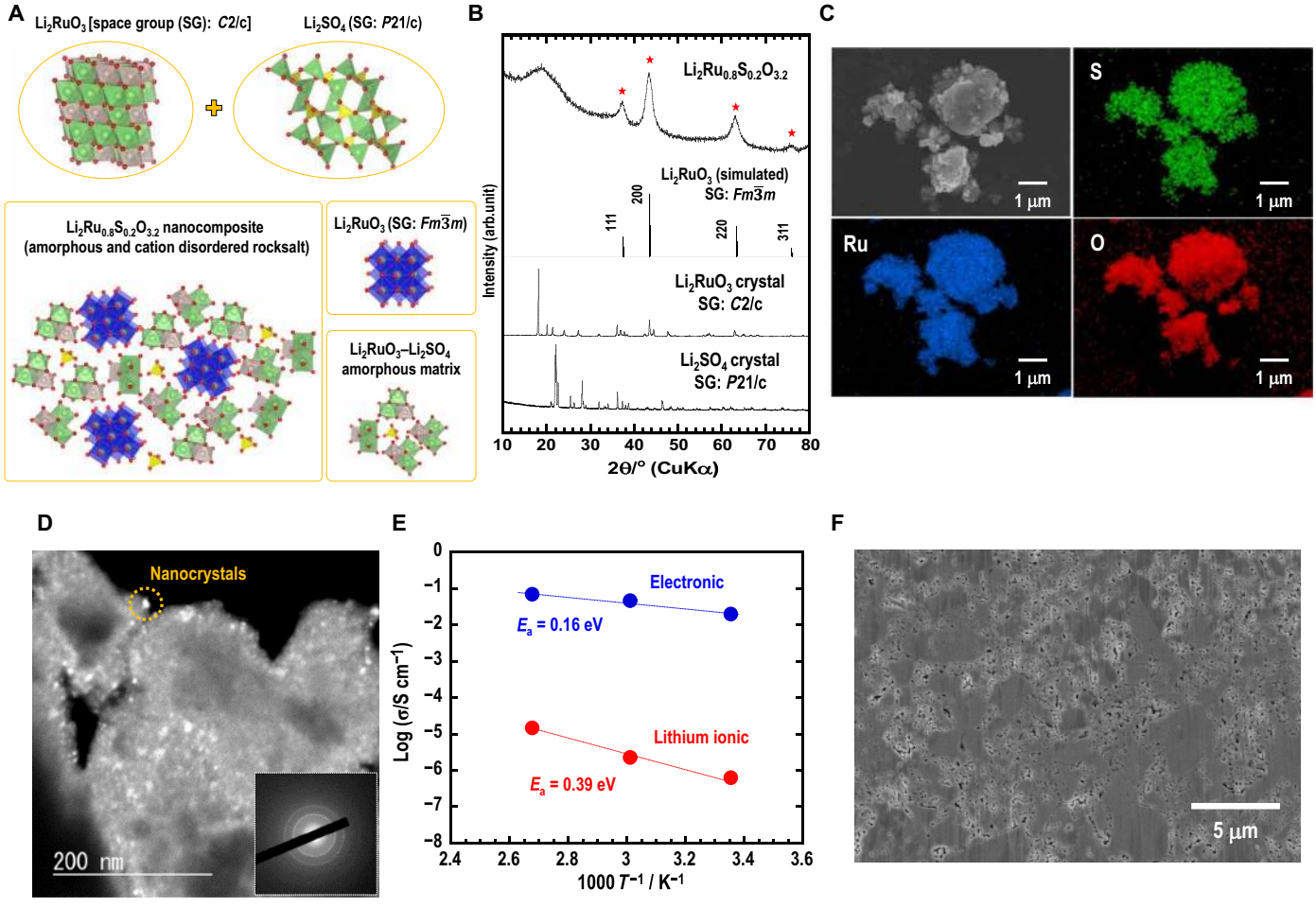

Fig. 1. Synthesis of the $Li_2Ru_{0.8}S_{0.2}O_{3.2}$ positive electrode active material. (**A**) Schematic image for the synthesis strategy of Li_2RuO_3-Li_2SO_4 positive electrode active materials via mechanochemistry from Li_2RuO_3 [space group (SG): *C*2/*c*] and Li_2SO_4 (SG: *P*21/*c*) crystals. (**B**) XRD patterns of $Li_2Ru_{0.8}S_{0.2}O_{3.2}$ after the mechanochemical synthesis. Cation-disordered Li_2RuO_3 crystal (SG: $Fm\bar{3}m$) has not been reported to date; therefore, the XRD pattern of the cubic structure was simulated with RIETAN-FP (*36*) and VESTA (*37*). (**C**) SEM image and corresponding EDX mappings for Ru, S, and O elements in $Li_2Ru_{0.8}S_{0.2}O_{3.2}$ powders. (**D**) DF-TEM image for $Li_2Ru_{0.8}S_{0.2}O_{3.2}$ particles and the corresponding ED pattern (inset). The bright spots in the DF-TEM image show the cation-disordered Li_2RuO_3 nanocrystalline region. Nanosized crystalline particles were dispersed in the amorphous Li_2RuO_3-Li_2SO_4 matrix. The ED pattern also indicates that these crystals have a cation-disordered rocksalt structure with the space group of $Fm\bar{3}m$. (**E**) Temperature dependence of the electronic (blue circles) and lithium ionic conductivity (red circles) for the $Li_2Ru_{0.8}S_{0.2}O_{3.2}$ electrode material. (**F**) Cross-sectional SEM image of the $Li_2Ru_{0.8}S_{0.2}O_{3.2}$ pellet pressed under 540 MPa at room temperature. Cross section of the pellet was polished by an argon ion milling system.

electron microscopy (SEM) image indicates that the particle size of the as-synthesized powder is approximately 0.1 to 5 μm, and energy-dispersive X-ray spectroscopy (EDX) mappings reveal that Ru, S, and O elements homogeneously distribute in the particles (Fig. 1C), indicating that Li_2RuO_3 and Li_2SO_4 are blended in nanometer size. Figure 1D shows a dark-field (DF) transmission electron microscopy (TEM) image and the corresponding electron diffraction (ED) pattern for $Li_2Ru_{0.8}S_{0.2}O_{3.2}$ particles. The DF-TEM image shows that nanosized cubic Li_2RuO_3 ($Fm\bar{3}m$) crystals (bright spots, ca. 20 nm) are embedded in the amorphous Li_2RuO_3-Li_2SO_4 matrix (dark area), as indicated by a bright contrast and marked with the dotted circle. The observed Debye rings in the ED pattern likewise support that the crystalline phase is assigned to the disordered rocksalt phase, as shown in fig. S2. It is noteworthy that the synthesized material is not just a mixture of Li_2RuO_3 crystal and Li_2SO_4 amorphous matrix—the nanocomposite material consists of the nanosized disordered rocksalt-type Li_2RuO_3 crystals and the amorphous Li_2RuO_3-Li_2SO_4 matrix.

Electrical conductivity and ductility of Li_2RuO_3-Li_2SO_4 electrode materials

Electronic and lithium ionic conductivities of $(100 - x)Li_2RuO_3 \cdot xLi_2SO_4$ (mol %) were evaluated using electrochemical techniques (figs. S3 and S4). Temperature dependence of electronic and ionic conductivities of $Li_2Ru_{0.8}S_{0.2}O_{3.2}$ ($x = 20$) is shown in Fig. 1E. At room temperature, electronic and ionic conductivities were 2.0×10^{-2} S cm^{-1} and 6.3×10^{-7} S cm^{-1}, respectively. $Li_2Ru_{0.8}S_{0.2}O_{3.2}$ is a mixed conductor with sufficiently high electronic conductivity and relatively high lithium ionic conductivity comparable to that of oxide glass solid electrolytes (*18*). In particular, activation energy for the ionic conduction (about 0.39 eV) in $Li_2Ru_{0.8}S_{0.2}O_{3.2}$ is relatively low among oxide-based lithium ionic conductors (*18*, *21*). This indicates that a favorable ionic conduction pathway has been created by the amorphization with Li_2SO_4. Because of this low activation energy, lithium ions can easily be extracted or inserted at the charging/discharging. It is considered that the enhancement of the ionic conductivity results from the open and random structure in the amorphous structure. In addition to the structure, the addition of Li_2SO_4 is important for the increase of the conductivity in the powder-compressed pellet. As shown in the cross-sectional SEM image of a green compact of $Li_2Ru_{0.8}S_{0.2}O_{3.2}$ (Fig. 1F), densification (i.e., "room temperature pressure-sintering") proceeds just by pressing at room temperature, which is a phenomenon usually seen in ductile sulfide solid electrolytes (*22*). Small voids still exist in the powder-compressed pellet, and the relative density of the pellet is about 64% (2.78 g cm^{-3}), which is calculated by using the powder density of $Li_2Ru_{0.8}S_{0.2}O_{3.2}$ (4.35 g cm^{-3}). This relative density is not sufficiently high, and there is a possibility to enhance the lithium ionic conductivity of $Li_2Ru_{0.8}S_{0.2}O_{3.2}$ by reducing the grain boundary resistance by further densification. However, in comparison with disordered Li_2RuO_3, the ionic conductivity of $Li_2Ru_{0.8}S_{0.2}O_{3.2}$ is more than one order of magnitude higher, which implies that the presence of Li_2SO_4 in the amorphous matrix is quite important to improve conduction properties of active materials (fig. S4).

All-solid-state cells using Li_2RuO_3-Li_2SO_4 positive electrode active materials

All-solid-state cells were assembled by pressing powders of the Li_3PS_4 glass electrolyte and Li_2RuO_3-Li_2SO_4 active materials at room temperature (fig. S4). For the positive electrode layer, only Li_2RuO_3-Li_2SO_4 active materials were applied with no conductive additives such as solid electrolytes and carbons, because the active material exhibited high electronic and ionic conductivities (Fig. 2A). As shown in fig. S4, where the cross-sectional SEM image for the electrode layer based on $Li_2Ru_{0.8}S_{0.2}O_{3.2}$ is described, a thick electrode is the favorable configuration for the high gravimetric and volumetric energy densities. The all-solid-state cell based on such a thick $Li_2Ru_{0.8}S_{0.2}O_{3.2}$ positive electrode functions as a secondary battery at 100°C, showing large reversible capacity of around 270 mAh g^{-1} (Fig. 2B). This reversible capacity is much larger than the theoretical capacity expected by the charge compensation of cationic Ru^{4+}/Ru^{5+} redox species in $Li_2Ru_{0.8}S_{0.2}O_{3.2}$ (141 mAh g^{-1}), which indicates that the extra capacity stems from other anionic redox species such as oxide ions. On the other hand, layered Li_2RuO_3 ($C2/c$) active material exhibited reversible capacity of ca. 170 mAh g^{-1} at the 10th cycle even in the composite positive electrode with a Li_3PS_4 glass electrolyte (fig. S5). This capacity is almost matched with the theoretical capacity of the cationic Ru^{4+}/Ru^{5+} redox reaction. Moreover, the cell based on the disordered Li_2RuO_3 ($Fm\bar{3}m$) active material shows limited capacity of ca. 80 mAh g^{-1}, indicating that the amorphous matrix based on Li_2SO_4 is effective for achieving higher capacity. As mentioned above, amorphization with Li_2SO_4 markedly improved the ductility and the ionic conductivity, which deliver the excellent battery performance. Moreover, it is notable that obvious voltage plateau due to the oxygen oxidation reaction was not observed for the $Li_2Ru_{0.8}S_{0.2}O_{3.2}$ positive electrode material in the initial charging. It is reported that in a highly crystalline active material such as Li_2RuO_3 and lithium-excess transition metal oxide electrodes, a clear plateau due to oxidation of oxide ions is confirmed. On the other hand, there are few reports of oxygen redox in amorphous materials. However, it is thought that the difference in structure determines the presence or absence of plateau generation. In the cation redox of an amorphous material such as V_2O_5, a clear plateau does not appear and a slope-like charge-discharge curve is obtained. The clear plateau does not appear in the all-solid-state battery using the active material synthesized this time, indicating that most of the active material is amorphous and the amorphous region functions as the active material. Furthermore, rate performance of the $Li_2Ru_{0.8}S_{0.2}O_{3.2}$ positive electrode material was also investigated (Fig. 2, C to F). Regrettably, because the active material showed moderate conductivity of about 10^{-5} S cm^{-1} even at 100°C for the high rate operating, the capacity linearly decreased with increasing operation current density. Thus, the challenge to improve the high rate performance by further increasing the ionic conductivity of the active material remains. Nevertheless, the cell exhibited an excellent cycle performance with high reversible capacity of about 200 mAh g^{-1} under the current density of 0.64 mA cm^{-2} (0.07 C). This capacity exceeds the theoretical capacity (141 mAh g^{-1}) generated from the Ru^{4+}/Ru^{5+} redox reaction, and thus, the oxygen redox reaction is reversibly used for long cycles. Coulombic efficiency during cycling was almost 99.9%, indicating high reversibility. However, energetic efficiency was about 79% due to the large polarization. Figure 2H shows the charge-discharge curves of the all-solid-state cell at the 25th, 40th, 50th, and 60th cycles operated under 0.64 mA cm^{-2} (0.07 C) at 100°C. Although only a slight capacity fading was observed, all the curves are overlapping and obvious voltage decay was not observed. These results reveal the high reversibility of the Li_2RuO_3-Li_2SO_4 positive electrode in all-solid-state cells.

To increase energy density based on the total battery weight, we applied a lithium metal negative electrode instead of the Li-In alloy

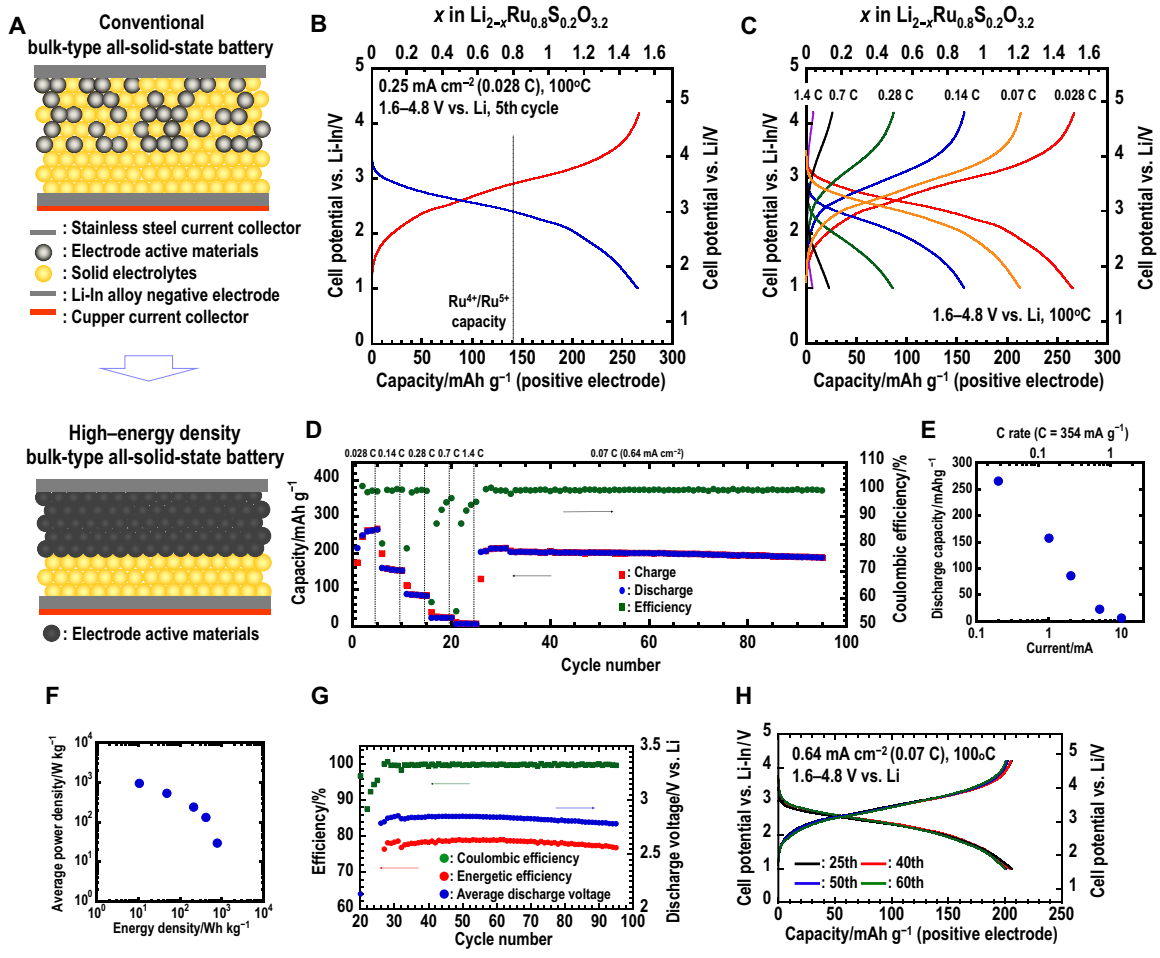

Fig. 2. Charge-discharge profile for bulk-type all-solid-state cell with the monolithic $Li_2Ru_{0.8}S_{0.2}O_{3.2}$ positive electrode. (**A**) Schematic for high energy density of bulk-type all-solid-state batteries. Typical bulk-type all-solid-state batteries are composed of the composite positive electrode, solid electrolyte, and lithium-indium alloy negative electrode layers. Especially in the composite positive electrode layer, active material contents should be increased to improve the energy density of battery. The positive electrode layer composed only of active material is the most ideal battery configuration for high energy density. (**B**) Charge-discharge curves of the all-solid-state cell operated under the constant current density of 0.25 mA cm^{-2} (0.028 C rate) at 100°C. (**C**) Charge-discharge performance under the operation of various current densities. (**D**) Cycle performance of the bulk-type all-solid-state cell. (**E**) Relationship between current density and discharge capacity. C rate (C = 354 mA g^{-1}) is defined by the theoretical capacity when all the lithium ions are extracted from the $Li_2Ru_{0.8}S_{0.2}O_{3.2}$ positive electrode active material. (**F**) Relationship between energy density and average power density based on the weight of the positive electrode. (**G**) Relationship between coulombic/energetic efficiencies, average discharge voltage, and cycle number for an all-solid-state cell operated at 0.07 C (0.64 mA cm^{-2}) at 100°C. (**H**) Charge-discharge curves at the 25th, 40th, 50th, and 60th cycles.

(fig. S6). Furthermore, to improve the lithium dissolution/deposition performance without short-circuiting, a gold thin film was inserted at the Li/Li_3PS_4 interface (*23*). The all-solid-state lithium metal cell functioned stably as a secondary battery. This solid-state cell configuration ($Li/Li_3PS_4/Li_2Ru_{0.8}S_{0.2}O_{3.2}$) is a favorable one for high energy density, exhibiting an energy density of 220 Wh kg^{-1} based on cell weight excluding current collectors.

Electrochemical analysis of the $Li_2Ru_{0.8}S_{0.2}O_{3.2}$ positive electrode in charging-discharging processes

To evaluate the thermodynamics and kinetics of the redox reaction in $Li_2Ru_{0.8}S_{0.2}O_{3.2}$, we carried out electrochemical analyses. Results of the galvanostatic intermittent titration test (GITT) and the corresponding AC impedance measurement for the initial and second charge-discharge states are shown in Fig. 3 and fig. S7. The diffusion coefficient ($D \cdot R^{-2}$) was calculated from GITT curves as referred to in the previous reports (*13*, *24*). In the early charging state where cationic oxidation reaction mainly occurs, charge transfer resistance (R_{ct}) increased and $D \cdot R^{-2}$ decreased with an increase of charge. In the latter charging state where anionic oxidation occurs, R_{ct} almost did not change, while $D \cdot R^{-2}$ markedly decreased, which means that ionic diffusion in the electrode layer is the rate-limiting step during anionic oxidation. In the conventional composite electrode with layered Li_2RuO_3 shown in fig. S5, on the other hand, interfacial resistance exponentially increased in the anionic oxidation region. This is because the large charge transfer resistance between the sulfide electrolyte and the active material in the composite electrode layer inhibited ion migration at the interface (*25*, *26*). The rate-limiting step here is charge transfer reaction. The anionic oxidation reaction is inhibited because of the large charge transfer resistance, and high capacity could not be obtained in the composite electrode. Coating of the electrode active material particles with oxide electrolytes is

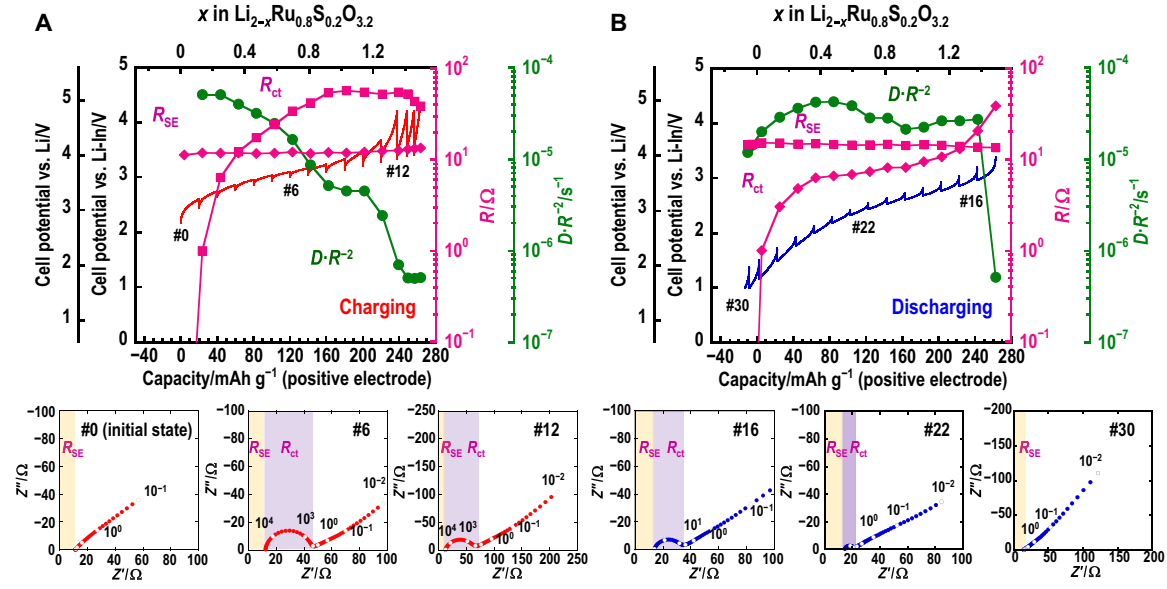

Fig. 3. Electrochemical analysis of the $Li_2Ru_{0.8}S_{0.2}O_{3.2}$ positive electrode active material during the initial charge-discharge process. GITT profiles (constant current charge in 0.25 mA cm^{-2} for 2 hours and OCV rest for 10 hours) (**A**) in charging state and (**B**) in discharging state. Resistance of solid electrolyte layer (R_{SE}) was determined by the real axis intercept in the high-frequency region in AC impedance plots. Charge transfer resistance (R_{ct}) is defined by the value of the semicircle observed in the middle frequency region with a capacitance of about 10^{-6} F. Mean diffusion coefficient ($D \cdot R^{-2}$) is calculated from the GITT profiles.

effective in achieving large reversible capacity by decreasing the interfacial resistance in the composite electrode with crystalline active materials (*27*). On the other hand, in the cell using the monolithic $Li_2Ru_{0.8}S_{0.2}O_{3.2}$ positive electrode, the amorphous Li_2RuO_3-Li_2SO_4 matrix functioned as an ionic conduction pathway, i.e., as a solid electrolyte in the electrode layer. Because of the lower electrochemical potential gap in oxide-based electrolytes and the oxide electrode, charge transfer resistance decreased and better battery performance was obtained. In the corresponding discharge state, R_{ct} and $D \cdot R^{-2}$ changed by a different route from the charging state, demonstrated by the voltage hysteresis in the charge-discharge curves. It must be noted that excess lithium has been inserted in the latter discharging state. This phenomenon was observed in other mechanically prepared disordered rocksalt materials (*28*). We believe that the presence of some amorphous matrix is expected in mechanically synthesized materials, providing additional stable sites for lithium ions on the basis of the open and random structure such that additional capacity can potentially be obtained. Hence, we believe that the additional lithium ions have been inserted to the amorphous matrix, that is, the matrix undergoes redox.

Structural evaluation for the $Li_2Ru_{0.8}S_{0.2}O_{3.2}$ active material during the charge-discharge process

Structural analysis was carried out for the $Li_2Ru_{0.8}S_{0.2}O_{3.2}$ active material with the aim to elucidate the mechanism behind the high reversibility during the charge-discharge processes. XRD patterns and TEM images reveal that amorphization of the disordered rocksalt phase occurred during the charging process, while the disordered phase reprecipitated during the discharging process (Fig. 4 and fig. S8). After charging, diffraction peaks attributable to the rocksalt phase disappeared from the XRD pattern, as shown in Fig. 4A. In the DF-TEM image and ED pattern after the fully charged state, the bright spots that had been observed in the pristine sample vanished, and only a halo pattern was observed. This suggests that lithium ions had been extracted from the disordered rocksalt phase, and the crystalline phase mainly functions as an active material. In the DF-TEM image and the ED pattern after discharging, furthermore, disordered rocksalt-type nanocrystals exhibiting bright spots reprecipitated by the insertion of lithium ions, as shown in Fig. 4B. The high-resolution (HR) image in Fig. 4C shows that nanocrystals reprecipitated after discharging are present in the amorphous Li_2RuO_3-Li_2SO_4 matrix. In the other disordered oxide materials reported so far, such amorphization has never been observed even after the extraction of lithium ions, and only a slight intensity decrease with a shift toward the higher angles was observed in XRD peaks (*14*–*17*). On the other hand, the structural change between disordered rocksalt and amorphous phases during the charge-discharge process was observed in sulfide-based Li_2TiS_3 disordered compounds (*29*, *30*). In the Li_2TiS_3 sulfide active material, when lithium ions are extracted during charging, sulfide ions adjacent to the lithium vacancy sites migrated forward to other sulfide ions, and S—S covalent bonds were generated. Amorphization occurred with the distortion associated with the sulfide anion redox reaction and corresponding sulfur migration. Thus, in our synthesized material, we believe that the oxygen oxidation reaction and the corresponding distortion due to the change in distance and angle of the Ru—O bond will trigger the amorphization of rocksalt structure. Moreover, as calculated from the weak diffraction peaks in the fully charged state, volumetric change in the crystalline phase was estimated to be small. This peak shift has not been observed in the cationic redox region, but it has been observed in the anionic redox region, which means that volumetric shrinking and amorphization occurred competitively by changes in Ru—O bonds. The resulting volumetric change is small, similar to other typical crystalline materials (*7*, *8*), and the presence of the Li_2RuO_3-Li_2SO_4 amorphous matrix is considered to further suppress the volumetric change in Li_2RuO_3 nanocrystals. Kim and Manthiram (*31*) reported that the amorphous manganese oxyiodide ($Li_{1.5}Na_{0.5}MnO_{2.85}I_{0.12}$) positive electrode material exhibited high capacity and excellent cyclability.

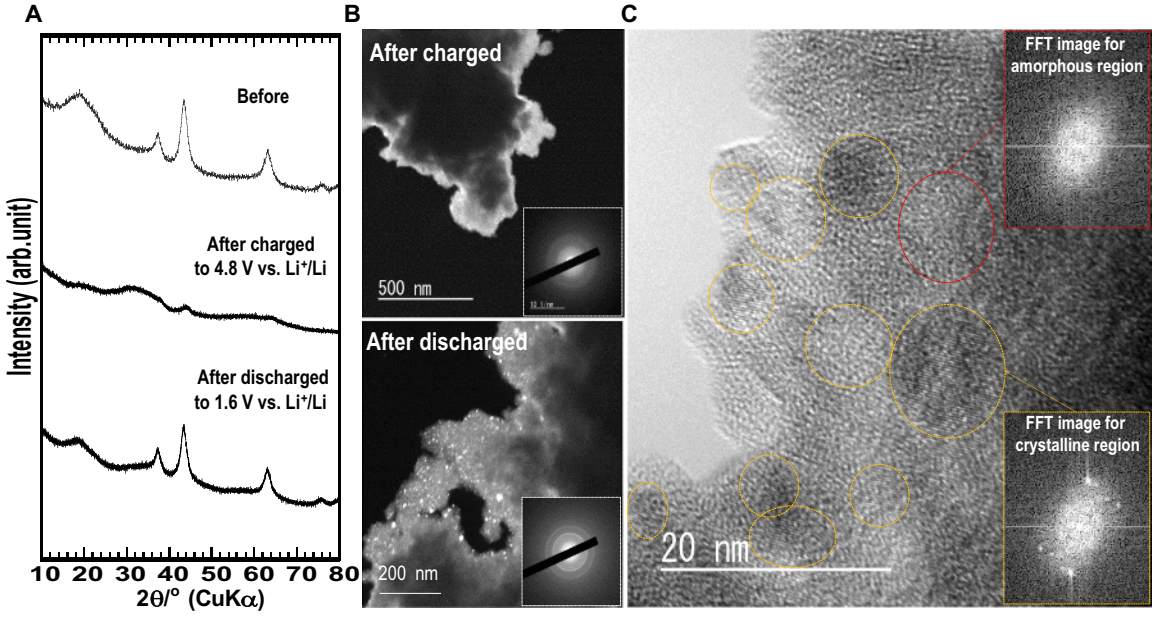

Fig. 4. Structural change of the $Li_2Ru_{0.8}S_{0.2}O_{3.2}$ positive electrode active material during the charge-discharge process. (**A**) Ex situ XRD patterns before and after the initial charge-discharge processes. (**B**) DF-TEM images and the corresponding ED pattern after the initial charge and discharge processes. (**C**) HR-TEM image for the $Li_2Ru_{0.8}S_{0.2}O_{3.2}$ positive electrode active material after the initial discharging. Nanosized cation-disordered rocksalt-type crystals are reprecipitated by the insertion of lithium ions, which are dispersed in the amorphous Li_2RuO_3-Li_2SO_4 matrix. The inserted figure shows the fast Fourier transform (FFT) images for the crystalline (yellow circle) and amorphous (red circle) regions in the $Li_2Ru_{0.8}S_{0.2}O_{3.2}$ active material after the initial discharge process.

The amorphous nature cooperates with the iodide anion to help to overcome the issues associated with lattice distortion, which is the reason behind the excellent cycle characteristics. In our material, the presence of the amorphous matrix with the SO_4^{2-} anion is likewise considered to ameliorate the battery cycle performance in all-solid-state cells. Thus, the choice of substitute anions is substantially important for achieving novel electrode materials with high capacity and cyclability.

Charge compensation mechanism of the $Li_2Ru_{0.8}S_{0.2}O_{3.2}$ positive electrode

To describe the charge compensation mechanism in $Li_2Ru_{0.8}S_{0.2}O_{3.2}$, we performed ex situ X-ray absorption spectroscopy (XAS). XAS spectra provide information about the electronic state and bonding character of the material. The XAS spectra for the $Li_2Ru_{0.8}S_{0.2}O_{3.2}$ active material at various charge states are illustrated in Fig. 5. Electronic states for as-prepared $Li_2Ru_{0.8}S_{0.2}O_{3.2}$ are discussed in the Supplementary Materials (fig. S9, A and B).

In the early charging state (0 to 66%), the absorption edge energy at the Ru *K*-edge shifts toward higher photon energy by charging (Fig. 5A). The same tendency is observed in the Ru *L*-edge X-ray absorption near-edge structure (XANES) spectra (Fig. 5C). These results indicate the oxidation of Ru during the charge reaction. However, as shown in Fig. 5B, the Fourier transform (FT) of the extended X-ray absorption fine structure (EXAFS) oscillation reveals that the local environment around Ru ions remains almost the same, indicating that the Ru—O bonding character is not notably altered in the $Li_2Ru_{0.8}S_{0.2}O_{3.2}$ active material. A study reported that the change in the FT peak of the nearest coordination number for RuO_2 was similarly small during lithiation, although the reported reaction is between Ru^{3+} and Ru^{4+} species (*32*). The capacity obtained here slightly exceeds the capacity expected in the Ru^{4+}/Ru^{5+} redox reaction, indicating some influence on the anion redox reaction, which we will discuss later on. These results indicate that the cationic Ru^{4+}/Ru^{5+} redox mainly occurs in the early charging state. Upon further charging (66 to 100%), the peak positions of the Ru *K*- and Ru *L*-edge do not change, which indicates that further oxidation of Ru ions (e.g., Ru^{5+}/Ru^{6+}) is negligible, and oxygen oxidation reaction mainly occurs. Moreover, the intensity of the pre-edge peak at around 22,120 eV in the Ru *K*-edge XANES spectra increased, indicating that the octahedral environment around Ru^{5+} ion has been changed. Furthermore, the drastic intensity decrease of the peak attributed to the Ru—O bond is observed in the EXAFS profile (Fig. 5B). The lowered intensity implies decrease of coordination number and/or increase of local distortion of the Ru—O bond. The coordination number of the Ru—O bond is constant, because capacity fading caused by oxygen release was not observed in Fig. 2. Therefore, we assume that the intensity decrease of the peak attributed to the Ru—O bond is caused by an increase in the local distortion of the Ru—O bond.

These results indicate that the bonding character changed as a result of oxidation of the oxide ions instead of the Ru ions. Although the bond length of the Ru—O bond is not changed markedly, the bonding is highly distorted because of the anion redox reaction, which is the reason behind amorphization occurring in the high charging state. In the corresponding discharge process (fig. S9, E and F), Ru *K*- and *L*-edge peaks are shifted back to a lower energy than that of the pristine state, meaning that Ru ions are significantly reduced by insertion of excess lithium, which also matches with the result in the charge-discharge curves.

Moreover, to investigate the electronic structural change around oxide ions, O *K*-edge XAS spectra were collected with soft X-ray

absorption measurement (Fig. 5D). The intensity of the peak at 530 eV decreased, and the intensity at 527 eV increased with increasing charge state. This spectral change demonstrates that electrons are extracted from highly hybridized O2p-Ru4d bonding. Once an electron is extracted from the Ru—O bond, the electron belonging to the oxygen atom is transferred to the Ru ion ($Ru^{6+} \rightarrow Ru^{5+}L$) because of the strong covalent character of O2p-Ru4d bonding. These results reflect a hole formation in the hybridized O2p-Ru4d orbital. This trend is almost similar to the previous report by Tarascon's group (*33*). In the discharged state, the characteristic peak at 527 eV in O *K*-edge spectra disappears with the insertion of excess lithium ions, which indicates that the holes generated during charging are fully occupied by electrons.

In addition, the spectral change in the S *K*-edge XAS spectra was also investigated (Fig. 5E). There are obvious intense peaks at 2482 eV in all the charge-discharge states, which suggests that most of the sulfur exists in the hexavalent state during the charge-discharge process. In addition, there is a broad peak at 2471 eV assigned to sulfide species (*34*). The intensity of this peak decreases during charging and increases during discharging. These results show that sulfide species are oxidized in the charging state and reduced in the discharging state, which also contributes to achieving high capacity. The theoretical electrochemical potential for the S^{2-}/S_2^{2-} redox reaction is 2.1 V versus Li. However, the capacity obtained in the low-voltage region is not so large, and thus, the contribution of the sulfur redox reaction is thought to be small. The feature observed at 2477 eV at the discharged state suggests the formation of SO_3^{2-} species. This implies the redox of the sulfate at the low-voltage region. Further studies are essential to elucidate this behavior.

XPS for the amorphous Li_2RuO_3-Li_2SO_4 matrix

We conducted X-ray photoelectron spectroscopy (XPS) measurements with the aim to describe the role of the SO_4^{2-} anion in the amorphous Li_2RuO_3-Li_2SO_4 matrix during charge-discharge states. In the O1s XPS spectra (Fig. 6A), the intensity of the peaks at 529 eV attributable to lattice oxygen in Li_2RuO_3 is decreased with increasing charge state. This result suggests that the electronic state change in the oxygen anion contributes to charge compensation. Although the binding energy of the lattice oxygen is not changed, that of the SO_4^{2-} anion is shifted to the lower energy side. Moreover, in the S2p spectra

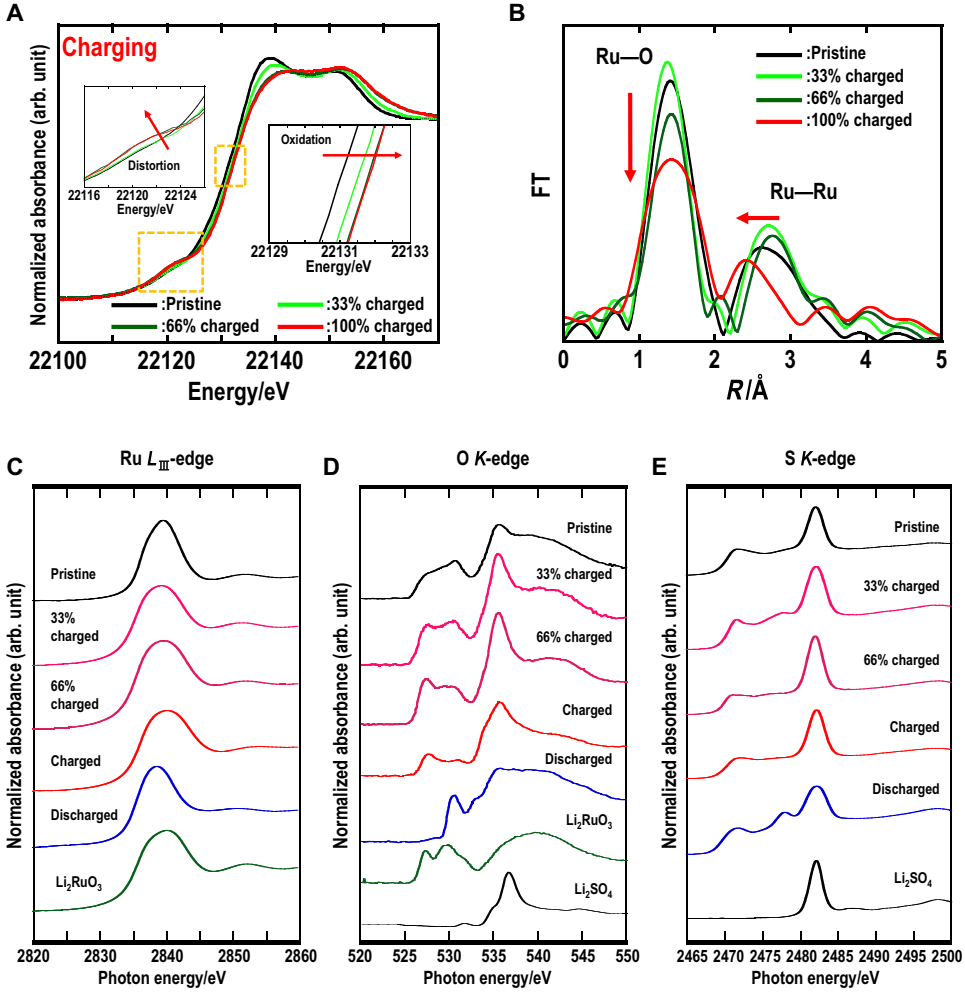

Fig. 5. Charge compensation mechanism for the $Li_2Ru_{0.8}S_{0.2}O_{3.2}$ positive electrode active material by XAFS measurements. (**A**) Ru *K*-edge XANES spectra. (**B**) EXAFS oscillations for $Li_2Ru_{0.8}S_{0.2}O_{3.2}$ in the charging state. (**C**) Ru L_{III}-edge XANES spectra. (**D**) O *K*-edge XANES spectra. (**E**) S *K*-edge XANES spectra for the $Li_2Ru_{0.8}S_{0.2}O_{3.2}$ active material after the charge-discharge measurement.

(Fig. 6B), doublet peaks assigned to SO_4^{2-} also shift toward a lower energy. These results mean that electron density around SO_4^{2-} anion increases even during the charging state. In the corresponding discharging state, this electron density energy returns to the lower energy levels. This unique peak shift can be used to monitor the charge state, because the SO_4^{2-} anion highly interacts with the Ru ion in the Li_2RuO_3-Li_2SO_4 amorphous matrix. In the amorphous matrix, the electron is withdrawn from the Ru ion through the inductive effect of the SO_4^{2-} anion (*35*), and electron density around SO_4^{2-} anion increases. The position of peaks in both O1s and S2p spectra for the SO_4^{2-} anion exists at higher binding energy than the pristine state, which means that excess lithium has been inserted to the amorphous matrix (Fig. 6C). Furthermore, in S2p spectra, the peaks generated by the amorphization with Li_2RuO_3, which was assigned to SO_3^{2-} (167 eV), polysulfide species S_2^{2-} and S^{2-} (161 to 163 eV), were gradually shifted to higher energies, and finally disappeared at the fully charged state, which is in accordance with the XAS results.

We propose the overall charge-discharge mechanism of $Li_2Ru_{0.8}S_{0.2}O_{3.2}$ in fig. S10. According to the detailed structural analysis by XRD and TEM, the obtained material is a nanocomposite where disordered Li_2RuO_3 crystals are dispersed into the Li_2RuO_3-Li_2SO_4 amorphous matrix. We conclude that the charge-discharge mechanism in the crystalline part is somewhat different from that in the amorphous part. In the disordered rocksalt region, capacity was obtained by charge compensation of cationic Ru^{4+}/Ru^{5+} and anionic O^{2-}/O^{-} redox reaction. On the other hand, in the amorphous region, the contribution of the S^{2-}/S^{n-} redox reaction has been observed in addition to these redox reactions. Moreover, in the latter discharge process, excess lithium has been inserted by the excess reduction in $Ru^{4+}/Ru^{3+\delta}$. Thus, the cationic $Ru^{3+\delta}/Ru^{5+}$ and anionic O^{2-}/O^{-} and S^{2-}/S^{n-} redox reactions take place in the amorphous matrix. The redox reactions in both crystalline and amorphous regions progress concurrently, and the high capacity of 270 mAh g^{-1} is obtained in the all-solid-state cell using the monolithic $Li_2Ru_{0.8}S_{0.2}O_{3.2}$ positive electrode.

In conclusion, a novel $Li_2Ru_{0.8}S_{0.2}O_{3.2}$ positive electrode active material was synthesized by a mechanochemical technique. The active material was a mixed conductor with an extremely high electronic conductivity and a relatively high lithium ionic conductivity. The all-solid-state cell using the $Li_2Ru_{0.8}S_{0.2}O_{3.2}$ positive electrode active material showed the high reversible capacity of 270 mAh g^{-1} because of the cumulative ruthenium, oxygen, and sulfur charge compensations, showing a unique charge-discharge mechanism between cation-disordered rocksalt crystal and the amorphous portion. The formation of the amorphous matrix with Li_2SO_4 provides the good ionic conduction pathway and favorable ductility to form a dense electrode layer. Amorphization with Li_2SO_4 is a promising strategy for designing high-capacity electrode active materials. Unfortunately, ruthenium compounds are too expensive to be commercialized. In this study, we have developed Li_2RuO_3-Li_2SO_4 as a model electrode for the construction of high–energy density ASSBs. Alternative electrode materials with inexpensive transition metal elements should be investigated. We believe that our approach will serve as a good guideline for the development of high-capacity electrode active materials.

MATERIALS AND METHODS

Synthesis of Li_2RuO_3-Li_2SO_4 positive electrode active materials

The Li_2RuO_3 crystal was synthesized from Li_2CO_3 (>99%; Wako Pure Chemical) and RuO_2 (99.9%; Sigma-Aldrich) by a typical solid-state reaction (*10*). A mixture of Li_2CO_3 (10% excess) and RuO_2 was put into Al_2O_3 crucible and then preheated at 900°C for 12 hours. The preheated sample was well ground by using an agate mortar and a pestle. The obtained powder was heated at 1150°C for 24 hours to obtain a well-crystallized Li_2RuO_3 sample. The Li_2SO_4 crystal was obtained by heat treatment of $Li_2SO_4{\cdot}H_2O$ (99.9%; Wako Pure Chemical) at 300°C for 3 hours in dry Ar atmosphere. The $Li_2Ru_{1-x}S_xO_{3+x}$ (x = 0, 0.1, 0.2, 0.3, 0.4, and 0.5) positive electrode active materials were synthesized by mechanical milling using a planetary ball-milling apparatus (Pulverisette 7; Fritsch). A mixture of Li_2RuO_3 and Li_2SO_4 crystals was used as a precursor for milling. The mixture was put into a 45-ml zirconia pot with 160 balls (5 mm in diameter) and milled at a rotating speed of 370 rpm with a milling time of 50 hours. All processes were conducted in dry Ar atmosphere.

Synthesis of Li_3PS_4 glass electrolyte

Li_3PS_4 glass electrolyte was also prepared using mechanical milling (*22*, *23*, *25*). A mixture of Li_2S (99.9%; Mitsuwa Chem. Co. Ltd.) and P_2S_5 (99%; Sigma-Aldrich) was put into a 225-ml zirconia pot with 2500 zirconia balls (4 mm in diameter) and milled at a rotating speed of 210 rpm with a milling period of time of 45 hours using a planetary ball-milling apparatus (Pulverisette 5; Fritsch). All processes were conducted in dry Ar atmosphere to avoid the effects of moisture.

XRD measurement

XRD patterns were recorded using a diffractometer (SmartLab; Rigaku Corp.) equipped with a CuKα radiation source and a detector (Dtex2000) and operated at 45 kV and 200 mA. Rietveld analysis was carried out with RIETAN-FP (*36*). The structural model was fabricated using VESTA (*37*).

Powder density measurement

Densities of the synthesized powders were measured using an argon gas pycnometer (AccuPycII 1340; Shimadzu Corp.) placed in an Ar-filled glove box. Powder density was treated as including the closed pore in the particles. Relative density of the compressed pellet was calculated by dividing the apparent density by the powder density of the Li_2RuO_3-Li_2SO_4 active materials.

FE-SEM and EDX measurements

The morphology of the prepared samples was observed using a field-emission (FE)–SEM (SU8220; Hitachi High-Technologies Corp.). Distribution of the Ru, S, and O elements in the particles was investigated by using an EDX (EMAX Evolution; Horiba Ltd.) with acceleration voltages of 15 kV at room temperature. In addition, SEM images for the cross section of the compressed $Li_2Ru_{1-x}S_xO_{3+x}$ pellets were observed to investigate the deformability of the active material. The obtained $Li_2Ru_{1-x}S_xO_{3+x}$ powders were uniaxially pressed under 540 MPa at room temperature, and the active material pellets were collected. The pellets were divided, and the cross sections were polished using an argon ion milling system (IM4000; Hitachi High-Technologies Corp.). They were then observed by FE-SEM.

TEM observation

TEM observation was performed using JEM-2100F FE-type TEM systems (JEOL) with acceleration voltages of 200 kV at room temperature. To avoid the effects of moisture from the air, a double-tilt vacuum transfer TEM folder (Gatan model 648) was used during the observation. The nanostructures for the synthesized materials

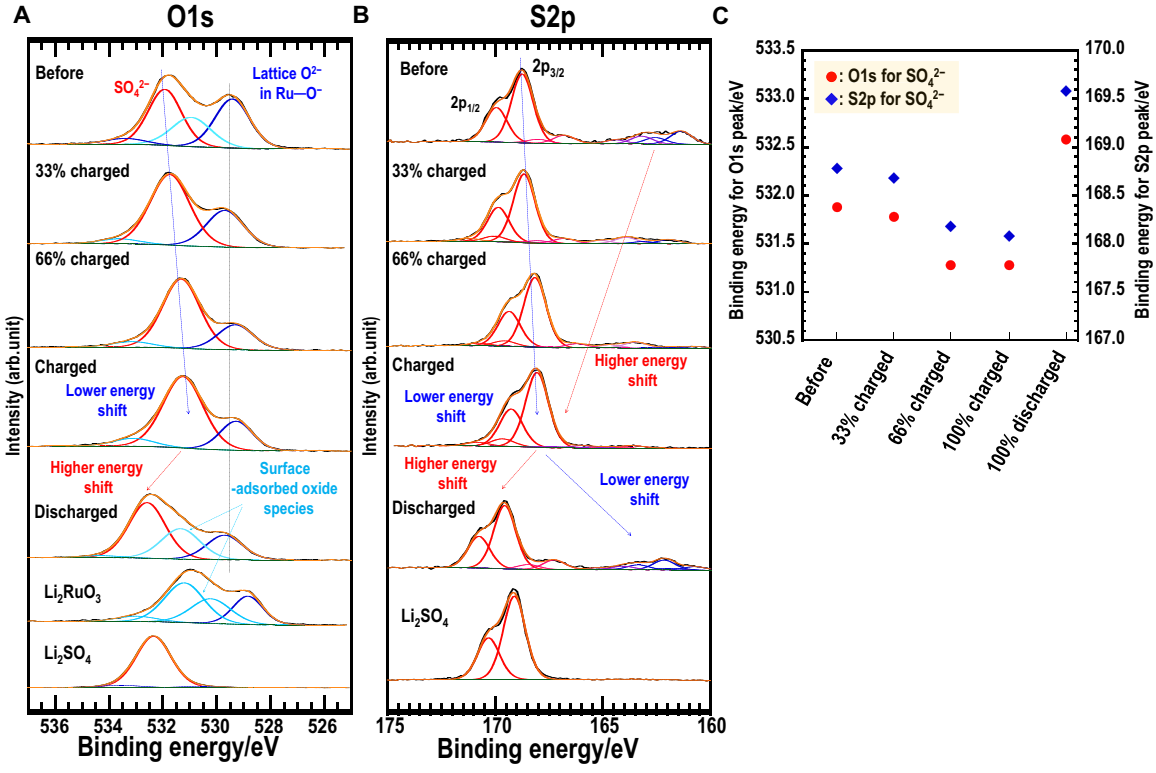

Fig. 6. Electronic structural analysis for the $Li_2Ru_{0.8}S_{0.2}O_{3.2}$ positive electrode active material during the charge-discharge process by XPS. All peaks were calibrated with the peak position of $Au4f_{7/2}$ to 84.0 eV. (**A**) O1s XPS spectra. (**B**) S2p XPS spectra for the $Li_2Ru_{0.8}S_{0.2}O_{3.2}$ positive electrode active material. As a reference, the spectra for the crystalline Li_2RuO_3 and Li_2SO_4 were also recorded. In the O1s spectra, there are three characteristic peaks. The peak at the lowest energy side (dark blue) is assigned to lattice oxygen in the Li_2RuO_3 structure. The peak at the higher energies (red) denotes the oxygen in the sulfate anion. The peak in the middle is presumably due to the surface-adsorbed oxide species such as carbonate. In particular, the peak attributed to the peroxo-like $(O—O)^{n-}$ species has not been confirmed in the charged state; its position overlaps with the peak of the sulfate. (**C**) Summary of the peak positions in O1s and S2p XPS spectra for the sulfate anion during the charge-discharge process.

were investigated by capturing HR-TEM images, DF images, and corresponding ED patterns. To visualize the distribution and size of nanocrystallites, hollow-cone DF-TEM imaging technique was applied (*38*). In this technique, the incident electron beam is tilted at a fixed angle and rotated with respect to the optical axis of the objective lens. Beam rotation is conducted automatically via the microscope control software. The diffraction spots in the ED pattern can be accurately reflected in the DF image as a bright-contrast region. Samples were mounted on an amorphous carbon film supported by a Cu grid for TEM observation, which was then attached to a TEM holder in a dry Ar–filled glove box. The vacuum pressure in TEM was approximately 1.0×10^{-5} Pa.

X-ray absorption spectroscopy

XAS measurements were conducted for the $Li_2Ru_{0.8}S_{0.2}O_{3.2}$ positive electrode active material to identify the electronic structural changes during the charge-discharge measurement. X-ray absorption spectra at the Ru *K*-edge were measured in the transmission mode at BL14B2 of SPring-8. The X-ray from the storage ring was monochromated by a Si (111) crystal. Moreover, the soft X-ray absorption measurements were performed at the SR Center, Ritsumeikan University. The spectra at O *K*-edge were measured at BL-2 with a grating monochromator, and the spectra at Ru *L*-edge and S *K*-edge were measured at BL-10 with a Ge (111) double-crystal monochromator. These soft X-ray absorption spectra were recorded in total electron yield mode, wherein the sample current produced by the excitation of electrons of different energies was measured. The samples for the soft X-ray absorption measurements were mounted on a sample stage in a dry argon–filled glovebox and transferred to the chamber using an argon-filled transfer vessel without exposure to air.

X-ray photoelectron spectroscopy

XPS measurements were conducted using K-Alpha (Thermo Fisher Scientific Inc.) with a Monochromatic Al Kα source (1486.6 eV) to investigate the charge-discharge mechanism of the positive electrode. The observed binding energies were calibrated with the $Au4f_{7/2}$ peak to 84.0 eV, because the adventitious C1s peak was overlapped with the Ru3d peaks. After the charge-discharge measurement, all-solid-state cells were disassembled, and then the samples were mounted on a sample stage in a dry Ar–filled glove box. They were transferred to an analysis chamber using an Ar-filled transfer vessel.

Conductivity measurements

Electronic and ionic conductivities were measured for the $Li_2Ru_{1-x}S_xO_{3+x}$ active materials pressed under 540 MPa. The pellet diameter and thickness were 10 mm and about 0.5 mm, respectively. Electronic and lithium ionic conductivities were measured using the AC impedance and DC polarization methods. Electronic conductivity measurement was performed for the pellets [Au/$Li_2Ru_{1-x}S_xO_{3+x}$ (ca. 100 mg)/Au].

Au thin-film electrode was deposited on both faces of the $Li_2Ru_{1-x}S_xO_{3+x}$ pellets using a vacuum evaporation technique with a sputter apparatus (Quick Coater SC701MKII Advance; Sanyu Electron Corp.). To evaluate lithium-ion conductivity, three-layer pellets [Li_3PS_4 (80 mg)/$Li_2Ru_{1-x}S_xO_{3+x}$ (40 mg)/Li_3PS_4] were obtained by pressing the corresponding powders under 540 MPa at room temperature. Lithium-ion conducting Li_3PS_4 glass electrolyte was used as an electron-blocking layer because of its low electronic conductivity. Metallic Li foils (9 mmϕ, 0.25 mm thickness) were attached to both sides of the pellet. Five layers of pellets (Li/Li_3PS_4/$Li_2Ru_{1-x}S_xO_{3+x}$/Li_3PS_4/Li) were sandwiched by Cu foils to serve as a current collector. AC impedance measurements were conducted using an impedance analyzer (SI-1260; Solartron Analytical). The frequency range and the applied voltage were 100 kHz to 0.1 Hz and 50 mV, respectively. DC polarization measurements were also conducted for the same cells using a potentiogalvanostat (SI-1287; Solartron Analytical). After reaching the equilibrium, the electronic and ionic conductivities were calculated from the residual currents in the polarization curves, respectively.

Fabrication of all-solid-state cells

All-solid-state cells (Li-In/Li_3PS_4/$Li_2Ru_{1-x}S_xO_{3+x}$) were constructed to investigate the electrochemical performance of the prepared active material. Positive electrodes were composed of only the prepared $Li_2Ru_{1-x}S_xO_{3+x}$ active material powders without any solid electrolytes and conductive additives. Three-layer pellets consisting of the current collector, positive electrode, and separator layers were prepared by pressing the powders of stainless steel (SS) (ca. 200 mg), $Li_2Ru_{1-x}S_xO_{3+x}$ active materials (ca. 20 mg), and Li_3PS_4 glass (ca. 50 mg) under 540 MPa at room temperature for 5 min. SS powders were used as a current collector at the positive electrode for securing electronic conduction and mechanical strength of the pellet. The alloy negative electrode composed of indium foil (99.999%; 0.3 mm thickness; Furuuchi Chemical Corp.) and lithium foil (99.99%; 0.25 mm thickness; Furuuchi Chemical Corp.) and negative electrode current collector made of Cu foil were attached to the pellet. Then, the pellet was pressed at 120 MPa for 2 min to form a Li-In alloy negative electrode.

In addition, an all-solid-state cell using a layered Li_2RuO_3 crystal was fabricated to compare charge-discharge properties of the $Li_2Ru_{1-x}S_xO_{3+x}$ active materials. A mixture of the Li_2RuO_3 crystal [70 weight % (wt %)] and Li_3PS_4 glass electrolyte (30 wt %) was used as a composite positive electrode (ca. 25 mg). The mixture was obtained by hand-mixing using agate mortar and a pestle. The Li_3PS_4 glass powder was also used as an electrolyte layer (separator, ca. 50 mg). Lithium foil and indium foil were used to form a Li-In alloy negative electrode. These all-solid-state batteries were charged and discharged using a charge-discharge measuring device (580 Battery Test System; Scribner Associates Inc.) at 100°C. Furthermore, the galvanostatic intermittent titration technique was carried out to evaluate the thermodynamics and kinetics of active materials in charging and discharging states by using potentiogalvanostat [CellTest System (1470E); Solartron Analytical]. The constant current density of 0.25 mA cm^{-2} (0.056 C rate) for the charge of 20 mAh g^{-1} and the corresponding open circuit potential relaxation for 10 hours were applied. Afterward, AC impedance measurement was carried out to evaluate the interfacial resistance and diffusion properties in active materials. In the AC impedance measurement, the applied voltage and frequency region were 10 mV versus open circuit voltage (OCV) and 10^6 to 10^{-2} Hz, respectively.

Fabrication of high–energy density all-solid-state battery

All-solid-state batteries (Li/Au/Li_3PS_4/$Li_2Ru_{0.8}S_{0.2}O_{3.2}$) were constructed by the same procedure as described above. A gold thin film was deposited on the three-layer pellets (Li_3PS_4/$Li_2Ru_{0.8}S_{0.2}O_{3.2}$/SS) using a vacuum evaporation method. Then, metallic lithium and copper foils were attached and pressed at 80 MPa by using a cold isostatic pressing method. These all-solid-state batteries were charged and discharged using a charge-discharge measuring device (580 Battery Test System; Scribner Associates Inc.) at 100°C.

SUPPLEMENTARY MATERIALS

Supplementary material for this article is available at http://advances.sciencemag.org/cgi/content/full/6/25/eaax7236/DC1

REFERENCES AND NOTES

1. J.-M. Tarascon, M. Armand, Issues and challenges facing rechargeable lithium batteries. *Nature* **414**, 359–367 (2001).
2. J. Janek, W. G. Zeier, A solid future for battery development. *Nat. Energy* **1**, 16141 (2016).
3. A. Manthiram, X. Yu, S. Wang, Lithium battery chemistries enabled by solid-state electrolytes. *Nat. Rev. Mater.* **2**, 16103 (2017).
4. Y. Seino, T. Ota, K. Takada, A. Hayashi, M. Tatsumisago, A sulphide lithium super ion conductor is superior to liquid ion conductors for use in rechargeable batteries. *Energ. Environ. Sci.* **7**, 627–631 (2014).
5. N. Kamaya, K. Homma, Y. Yamakawa, M. Hirayama, R. Kanno, M. Yonemura, T. Kajiyama, Y. Kato, S. Hama, K. Kawamoto, A. Mitsui, A lithium superionic conductor. *Nat. Mater.* **10**, 682–686 (2011).
6. Y. Kato, S. Hori, T. Saito, K. Suzuki, M. Hirayama, A. Mitsui, M. Yonemura, H. Iba, R. Kanno, High-power all-solid-state batteries using sulfide superionic conductors. *Nat. Energy* **1**, 16030 (2016).
7. K. Mizushima, P. C. Jones, P. J. Wiseman, J. B. Goodenough, $LixCoO_2$ (0<x≤1): A new cathode material for batteries of high energy density. *Mater. Res. Bull.* **15**, 783–789 (1980).
8. T. Ohzuku, Y. Makimura, Layered lithium insertion material of $LiCo_{1/3}Ni_{1/3}Mn_{1/3}O_2$ for lithium-ion batteries. *Chem. Lett.* **30**, 642–643 (2001).
9. M. H. Rossouw, M. M. Thackeray, Lithium manganese oxides from Li_2MnO_3 for rechargeable lithium battery applications. *Mater. Res. Bull.* **26**, 463–473 (1991).
10. A. C. W. P. James, J. B. Goodenough, Structure and bonding in lithium ruthenate, Li_2RuO_3. *J. Solid State Chem.* **74**, 287–294 (1988).
11. M. Sathiya, A. M. Abakumov, D. Foix, G. Rousse, K. Ramesha, M. Saubanère, M. L. Doublet, H. Vezin, C. P. Laisa, A. S. Prakash, D. Gonbeau, G. VanTendeloo, J.-M. Tarascon, Origin of voltage decay in high-capacity layered oxide electrodes. *Nat. Mater.* **14**, 230–238 (2015).
12. M. Sathiya, G. Rousse, K. Ramesha, C. P. Laisa, H. Vezin, M. T. Sougrati, M.-L. Doublet, D. Foix, D. Gonbeau, W. Walker, A. S. Prakash, M. Ben Hassine, L. Dupont, J.-M. Tarascon, Reversible anionic redox chemistry in high-capacity layered-oxide electrodes. *Nat. Mater.* **12**, 827–835 (2013).
13. G. Assat, C. Delacourt, A. D. Corte, J.-M. Tarascon, Practical assessment of anionic redox in Li-rich layered oxide cathodes: A mixed blessing for high energy Li-ion batteries. *J. Electrochem. Soc.* **163**, A2965–A2976 (2016).
14. J. Lee, A. Urban, X. Li, D. Su, G. Hautier, G. Ceder, Unlocking the potential of cation-disordered oxides for rechargeable lithium batteries. *Science* **343**, 519–522 (2014).
15. D.-H. Seo, J. Lee, A. Urban, R. Malik, S. Kang, G. Ceder, The structural and chemical origin of the oxygen redox activity in layered and cation-disordered Li-excess cathode materials. *Nat. Chem.* **8**, 692–697 (2016).
16. N. Yabuuchi, M. Takeuchi, M. Nakayama, H. Shiba, M. Ogawa, K. Nakayama, T. Ohta, D. Endo, T. Ozaki, T. Inamasu, K. Sato, S. Komaba, High-capacity electrode materials for rechargeable lithium batteries: Li_3NbO_4-based system with cation-disordered rocksalt structure. *Proc. Natl. Acad. Sci. U.S.A.* **112**, 7650–7655 (2015).
17. N. Yabuuchi, M. Nakayama, M. Takeuchi, S. Komaba, Y. Hashimoto, T. Mukai, H. Shiiba, K. Sato, Y. Kobayashi, A. Nakao, M. Yonemura, K. Yamanaka, K. Mitsuhara, T. Ohta, Origin of stabilization and destabilization in solid-state redox reaction of oxide ions for lithium-ion batteries. *Nat. Commun.* **7**, 13814 (2016).
18. M. Tatsumisago, R. Takano, K. Tadanaga, A. Hayashi, Preparation of Li_3BO_3-Li_2SO_4 glass-ceramic electrolytes for all-oxide lithium batteries. *J. Power Sources* **270**, 603–607 (2014).
19. K. Nagao, A. Hayashi, M. Deguchi, H. Tsukasaki, S. Mori, M. Tatsumisago, Amorphous $LiCoO_2$-Li_2SO_4 active materials: Potential positive electrodes for bulk-type all-oxide solid-state lithium batteries with high energy density. *J. Power Sources* **348**, 1–8 (2017).

20. K. Nagao, A. Sakuda, A. Hayashi, H. Tsukasaki, S. Mori, M. Tatsumisago, Amorphous Ni-Rich $Li(Ni_{1-x-y}Mn_xCo_y)O_2$–$Li_2SO_4$ positive electrode materials for bulk-type all-oxide solid-state batteries. *Adv. Mater. Inter.* **6**, 1802016 (2019).
21. Y. Iriyama, T. Kako, C. Yada, T. Abe, Z. Ogumi, Charge transfer reaction at the lithium phosphorus oxynitride glass electrolyte/lithium cobalt oxide thin film interface. *Solid State Ion.* **176**, 2371–2376 (2005).
22. A. Sakuda, A. Hayashi, M. Tatsumisago, Sulfide solid electrolyte with favorable mechanical property for all-solid-state lithium battery. *Sci. Rep.* **3**, 2261 (2013).
23. A. Kato, M. Suyama, C. Hotehama, H. Kowada, A. Sakuda, A. Hayashi, M. Tatsumisago, High-temperature performance of all-solid-state lithium-metal batteries having Li/Li_3PS_4 interfaces modified with Au thin films. *J. Electrochem. Soc.* **165**, A1950–A1954 (2018).
24. K. M. Shaju, G. V. Subba Rao, B. V. R. Chowdari, Li ion kinetic studies on spinel cathodes, $Li(M_{1/6}Mn_{11/6})O_4$ (M = Mn, Co, CoAl) by GITT and EIS. *J. Mater. Chem.* **13**, 106–113 (2003).
25. A. Sakuda, A. Hayashi, M. Tatsumisago, Interfacial observation between $LiCoO_2$ electrode and Li_2S-P_2S_5 solid electrolytes of all-solid-state lithium secondary batteries using transmission electron microscopy. *Chem. Mater.* **22**, 949–956 (2010).
26. J. Haruyama, K. Sodeyama, L. Han, K. Takada, Y. Tateyama, Space-charge layer effect at interface between oxide cathode and sulfide electrolyte in all-solid-state lithium-ion battery. *Chem. Mater.* **26**, 4248–4255 (2014).
27. N. Ohta, K. Ohta, I. Sakaguchi, L. Zhang, R. Ma, K. Fukuda, M. Osada, T. Sasaki, $LiNbO_3$-coated $LiCoO_2$ as cathode material for all solid-state lithium secondary batteries. *Electrochem. Commun.* **9**, 1486–1490 (2007).
28. S. Hoshino, A. M. Glushenkov, S. Ichikawa, T. Ozaki, T. Inamasu, N. Yabuuchi, Reversible three-electron redox reaction of Mo^{3+}/Mo^{6+} for rechargeable lithium batteries. *ACS Energy Lett.* **2**, 733–738 (2017).
29. A. Sakuda, T. Takeuchi, K. Okamura, H. Kobayashi, H. Sakaebe, K. Tatsumi, Z. Ogumi, Rock-salt-type lithium metal sulphides as novel positive-electrode materials. *Sci. Rep.* **4**, 4883 (2015).
30. A. Sakuda, K. Ohara, T. Kawaguchi, K. Fukuda, K. Nakanishi, H. Arai, Y. Uchimoto, T. Ohta, E. Matsubara, Z. Ogumi, K. Kuratani, H. Kobayashi, M. Shikano, T. Takeuchi, H. Sakaebe, A reversible rocksalt to amorphous phase transition involving anion redox. *Sci. Rep.* **8**, 15086 (2018).
31. J. K. Kim, A. Manthiram, A manganese oxyiodide cathode for rechargeable lithium batteries. *Nature* **390**, 265–267 (1997).
32. Y.-Y. Hu, Z. Liu, K.-W. Nam, O. J. Borkiewicz, J. Cheng, X. Hua, M. T. Dunstan, X. Yu, K. M. Wiaderek, L.-S. Du, K. W. Chapman, P. J. Chupas, X.-Q. Yang, C. P. Gley, Origin of additional capacities in metal oxide lithium-ion battery electrodes. *Nat. Mater.* **12**, 1130–1136 (2013).
33. G. Assat, A. Iadecola, C. Delacourt, R. Dedryvère, J.-M. Tarascon, Decoupling cationic–anionic redox processes in a model Li-rich cathode via *Operando* x-ray absorption spectroscopy. *Chem. Mater.* **29**, 9714–9724 (2017).
34. F. Jalilehvand, Sulfur: Nota "silent" element any more. *Chem. Soc. Rev.* **35**, 1256–1268 (2006).
35. M. Saubanère, M. Ben Yahia, S. Lebègue, M.-L. Doublet, An intuitive and efficient method for cell voltage prediction of lithium and sodium-ion batteries. *Nat. Commun.* **5**, 5559 (2014).
36. F. Izumi, K. Momma, Three-dimensional visualization in powder diffraction. *Solid State Phenom.* **130**, 15–20 (2007).
37. K. Momma, F. Izumi, *VESTA 3* for three-dimensional visualization of crystal, volumetric and morphology data. *J. Appl. Cryst.* **44**, 1272–1276 (2011).
38. B. Yao, T. Sun, A. Warren, H. Heinrich, K. Barmak, K. R. Coffey, High contrast hollow-cone dark field transmission electron microscopy for nanocrystalline grain size quantification. *Micron* **41**, 177–182 (2010).
39. R. D. Shannon, Revised effective ionic radii and systematic studies of interatomic distances in halides and chalcogenides. *Acta Crystallogr.* **A32**, 751–767 (1976).
40. B. Raguenet, G. Tricot, G. Silly, M. Ribes, A. Pradel, The mixed glass former effect in twin-roller quenched lithium borophosphate glasses. *Solid State Ion.* **208**, 25–30 (2012).

Acknowledgments
Funding: This work was supported by JSPS KAKENHI grant number 18H05255. **Author contributions:** K.N. and Y.N. carried out the synthesis, electrochemical tests, and characterization. M.D. performed the XPS analyses. C.H. conducted XRD measurements and Rietveld refinements. H.T. and S.M. performed TEM observations. Y.O., K.Y., and Y.U. conducted the XAS measurements. A.S., A.H., and M.T. supervised the research. K.N. and A.S. wrote the manuscript. All authors took part in the discussion concerning experiments and the final manuscript. **Competing interests:** The authors declare that they have no competing interests. **Data and materials availability:** All data needed to evaluate the conclusions in the paper are present in the paper and/or the Supplementary Materials. Additional data related to this paper may be requested from the authors.

Submitted 16 April 2019
Accepted 23 April 2020
Published 19 June 2020
10.1126/sciadv.aax7236

Citation: K. Nagao, Y. Nagata, A. Sakuda, A. Hayashi, M. Deguchi, C. Hotehama, H. Tsukasaki, S. Mori, Y. Orikasa, K. Yamamoto, Y. Uchimoto, M. Tatsumisago, A reversible oxygen redox reaction in bulk-type all-solid-state batteries. *Sci. Adv.* **6**, eaax7236 (2020).

ScienceAdvances

A reversible oxygen redox reaction in bulk-type all-solid-state batteries

Kenji Nagao, Yuka Nagata, Atsushi Sakuda, Akitoshi Hayashi, Minako Deguchi, Chie Hotehama, Hirofumi Tsukasaki, Shigeo Mori, Yuki Orikasa, Kentaro Yamamoto, Yoshiharu Uchimoto and Masahiro Tatsumisago

Sci Adv **6** (25), eaax7236.
DOI: 10.1126/sciadv.aax7236

Science Advances (ISSN 2375-2548) is published by the American Association for the Advancement of Science, 1200 New York Avenue NW, Washington, DC 20005. The title *Science Advances* is a registered trademark of AAAS.